Three main physical phenomena, obtained by the PDA-measurements, can be summarized as direct results of a change in impingement height or a change in volume flow for both investigated ultrasonic atomizers. It was found that the inner core of each spray is defined by large values of the mean vertical drop velocities, as well as low values of the mean drop diameters and Sauter mean diameters. Due to the low drop diameters, the kinetic energies of the spray cores are relatively low.

For increasing impingement heights the regions with relatively high mean vertical drop velocities are found to increase, but simultaneously the maximum absolute values decrease due to the influence of the air drag forces on the drops. However, no clear change in the mean drop diameters or the Sauter mean diameters is observed, due to which the kinetic energies of the sprays have to decrease for increasing impingement heights.

In case of an increasing volume flow the regions where relatively high mean vertical drop velocities are measured, are found to increase with a simultaneous increase in the absolute maximum values of these vertical drop velocities. At the same time, the spray drop diameters and Sauter mean diameters increase as well. Both phenomena lead to strong increases of the kinetic energy distributions of the sprays for both ultrasonic atomizers.

The results of the surface film radial mean velocities and their fluctuations by means of $\mu - PIV$ show several interesting phenomena. The swirling motion of the spray comes clearly forward in the large vortices present in the surface films at both investigated impingement heights for both nozzles. The centers of these large vortices correspond to the centers of the impinging sprays. The carrier gas changes the swirl direction of the spray in such a way that sprays, obtained for both nozzles using the carrier gas, as well as the corresponding vortices inside the surface films are rotating in clockwise direction for both impingement heights, whereas the surface film vortices for impinging sprays without carrier gas are rotating in an anticlockwise sense.

For increasing impingement heights a clear decrease of the mean radial film velocities is found, as a result of a decrease of the mean vertical velocity of the sprays and the subsequent decrease of the kinetic energy. This results in a decrease of the radial film velocities induced by the cavities, appearing in the surface film at drop impingement.

For larger volume flows the areas with relatively high mean radial film velocities, as well as the values of the maximum absolute radial film velocities, are increasing, because an increase in volume flow is directly linked to an increase in the kinetic energy of the drops of the spray. However, no clear dependency of an increase in volume flow on the surface film mean radial velocity directions is found, nor a dependency of the impingement height on the directions of the streamlines or on the size and strength of the surface film vortices.

At radial positions of the surface film, where relatively high mean radial film velocities are observed, low values of the velocity fluctuations are found. For the regions in the surface film, where the flow is mainly in one of both directions, the velocity fluctuations in this particular direction are higher, whereas at the positions of saddle points and vortex cores the fluctuations in both directions are strong.

Part III: Three-dimensional Volumetric Micro Particle Image Velocimetry

Chapter 8

Volumetric Particle Image Velocimetry with two optical aberrations and a single camera

In §(6.2.2) the layout for the radial velocity measurements inside the surface film during spray impingement was explained. This chapter describes the applied measurement technique, the so-called volumetric Particle Image Velocimetry technique. This technique is based on micro-PIV and makes use of a single digital camera and two optical monochromatic aberrations, namely astigmatism and the spherical lens aberration. In this way, the particle position in depth can be encoded by using a combination of these two monochromatic aberrations.

A detailed overview of the different possible monochromatic and chromatic aberrations is given in §(8.1), followed by an explanation of the resulting optical imaging and the applied calibration method §(8.2). Out of the size and intensity distribution of the recorded particle images, the three-dimensional position of the particles inside the investigated flow volume can be determined. The different steps of this data processing will be discussed in §(8.3). To validate this new measurement technique, a laminar flow is being used, which is the topic of §(8.4).

8.1 Optical aberrations

Optical aberrations are defined as departures of the performance of an optical system from the predictions of the paraxial optics. This ideal imaging can only be achieved, when taking into account only the paraxial beams, i.e. those beams, which are close to the optical axis, having small angles with respect to this axis, Figure 8.1.

If this condition is satisfied, the values for the incident angles of the light rays, as well as the reflection and refraction angles, can be assumed to be small, i.e. the angle of the incident light ray, for example, defined by

$$\sin \epsilon = \epsilon - \frac{\epsilon^3}{3!} + \frac{\epsilon^5}{5!} - \ldots \approx \epsilon \tag{8.1}$$

$$\cos \epsilon = 1 - \frac{\epsilon^2}{2!} + \frac{\epsilon^4}{4!} - \ldots \approx 1 \tag{8.2}$$

can be approximated by its first term. When taking into account the second terms of the Taylor series for $sin(\epsilon)$ and $cos(\epsilon)$, the imaging errors of the 2nd and 3rd order are being introduced,
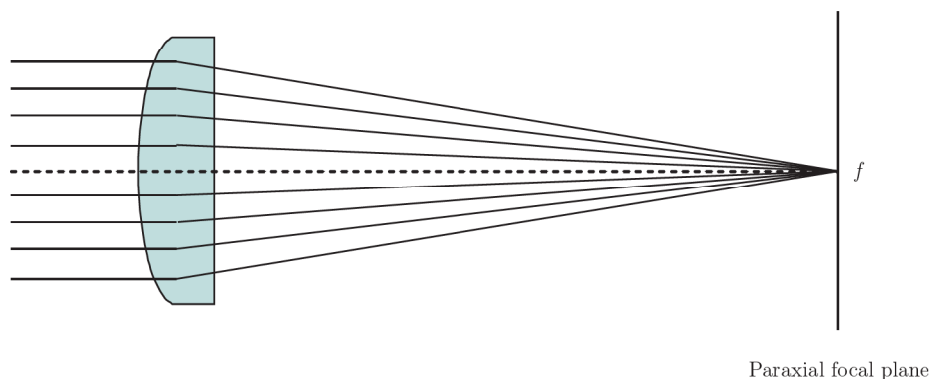
Figure 8.1: Aberration free imaging

the so-called optical aberrations. In general, these aberrations occur when light from one point of an object does not converge into a single point after having passed through the optical system.

Two different classes of aberrations can be defined: the monochromatic and the chromatic aberrations. The first class of aberrations is caused by the geometry of the lens and occurs both for reflected and refracted light. They appear even when monochromatic light is used. The different monochromatic aberrations are spherical lens aberrations, coma, astigmatism, field curvature and image distortion. Chromatic aberrations are caused by the variation of the refractive index of the lens for different wavelengths. These aberrations do not appear when monochromatic light is used. They can be divided into longitudinal and transverse chromatic aberrations.

8.1.1   Monochromatic optical aberrations

Rays of light proceeding from any object point in space unite in a corresponding image point, i.e. an object space is reproduced in an image space. The Gaussian theory, which permits the determination of the image of any object for any imaging system, is only valid as long as the angles made by all rays with the optical symmetry axis are infinitesimal small. This is usually only the case when the lenses, the objects and the images are infinitesimal small. In practice, however, these conditions are almost never realised, resulting in completely blurred images if the aperture of the imaging system exceeds a certain value. In this case, the different monochromatic aberrations can appear. In the next sections, the different monochromatic aberrations (spherical lens aberrations, coma, astigmatism, field curvature and image distortion) are explained in more detail.

Spherical lens aberration

Due to the spherical lens aberration incident rays near the edge of the lens, having a large lateral distance from the optical axis, will focus closer to the lens than incident rays close to the optical axis, the so-called paraxial rays, Figure 8.2.
The longitudinal spherical aberration is defined as the distance between the paraxial focal point f and the edge ray focal point, and is proportional to ρ^2, ρ being the diameter of the aperture. When the edge rays impinge on the paraxial focal plane, these imaging points are displaced from the paraxial point. This vertical distance is known as the transverse or lateral spherical
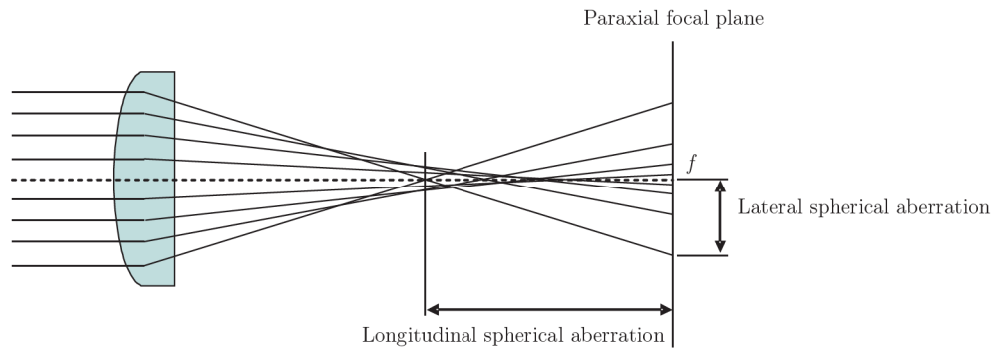
Figure 8.2: Principle of the spherical aberration

aberration and is proportional to ρ^3. The amount of spherical aberration depends, besides the lens aperture diameter, also on the lens shape and the index of refraction of the material of the lens.

Coma

For spherical lenses different regions of the lens surface exhibit different degrees of magnification, leading to coma, the next monochromatic aberration. Each concentric zone of the lens forms a so-called comatic circle, i.e. a ring-shaped image, Figure 8.3.
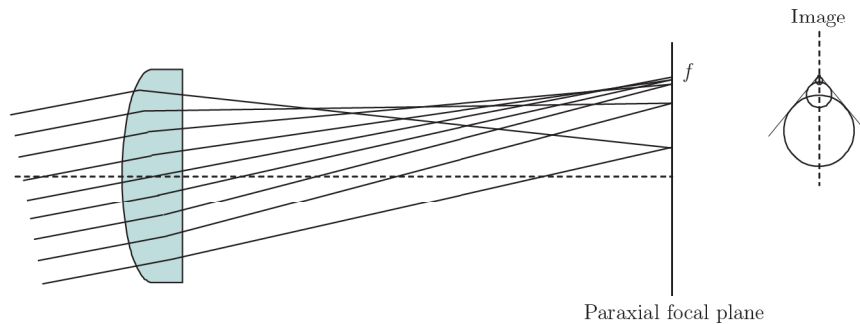

Figure 8.3: Monochromatic aberration coma

For off-axis object points, this leads to blurring of the image in the imaging plane, as the different zones of the lens do not focus the light at the same point. This results not in a sharp image point, as for the paraxial imaging, but it appears as a wedge-shaped point of light. The further off-axis the object or light source is, the stronger this effect appears.

Astigmatism

This aberration is manifested by the off-axis image of an object point, focussed by a spherical lens onto an image plane. The optical lens system appears to have two different focal points, Figure 8.4.
The object is imaged as a line or ellipse instead of a point. The plane containing both optical axes and the object point is called the tangential plane, whereas the plane perpendicular to this plane is the sagittal plane. Depending on the angle of the off-axis rays impinging on the
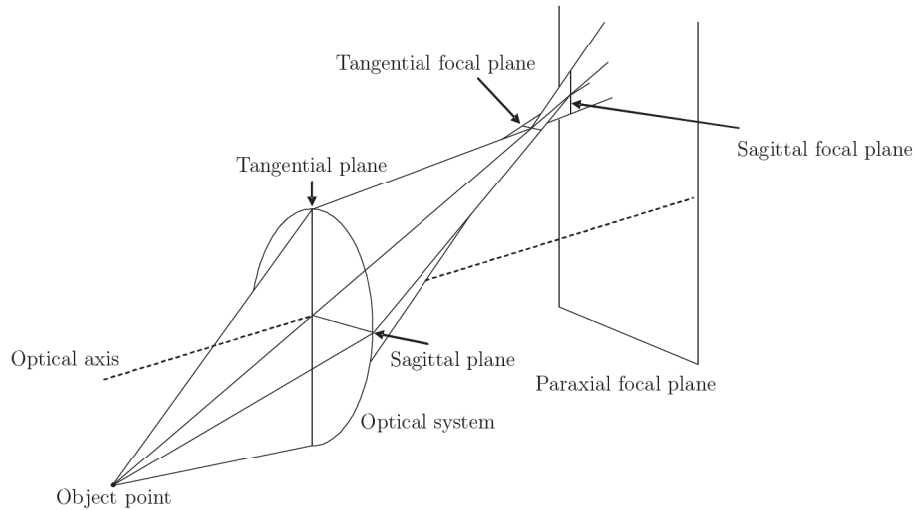
Figure 8.4: Principle of astigmatism

lens system, the line image may be oriented in either of the two directions. In this figure, the tangential rays come to a focus closer to the lens system than do rays in the sagittal plane. Between the two focal planes the image is either an ellipse or a circle, the latter one only when the imaging plane is placed in the point of least confusion.

The amount of astigmatism is defined as the distance between the two focal planes, Δ_s, and depends on the thickness of the lens t, the off-axis angle of the object θ and the index of refraction of the material of the lens n. Several equations can be found in literature to calculate this astigmatic distance:

$$[1] \quad \Delta_s = \frac{t}{\sqrt{n^2 - sin^2(\theta)}} \left[\frac{n^2 cos^2(\theta)}{n^2 - sin^2(\theta)} - 1 \right] \tag{8.3}$$

$$[2] \quad \Delta_s = \frac{t(n^2 - 1)sin^2(\theta)^2}{(n^2 - sin^2(\theta))^{3/2}} \tag{8.4}$$

and

$$[3] \quad \Delta_s \propto \frac{(n^2 - 1)t^3}{n^3} \tag{8.5}$$

Field curvature

In case the lens system is compensated for astigmatism, i.e. the sagittal plane and the tangential plane coincide, there is the tendency of the optical system to image objects better on a curved imaging surface than on a flat plate. This effect is called field curvature and its principle is sketched in Figure 8.5.
In the presence of astigmatism, due to two different focal planes, a curved image surface would compensate for this aberration. The amount of field curvature is depending on the refractive

---

[1]Melles Griot [97]
[2]Matsushita [92] and Smith [158]
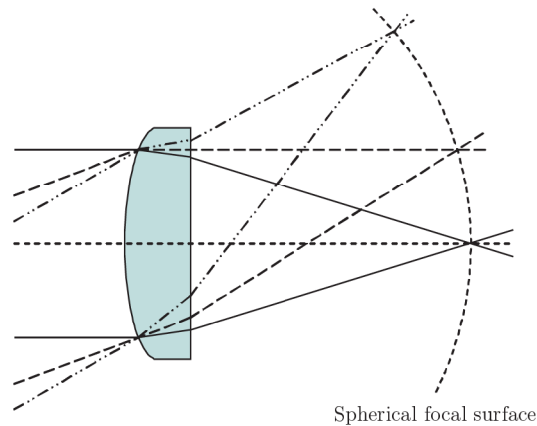[3]Fischer *et al.* [43]

226

Figure 8.5: Principle of field curvature

indices and focal distances of the applied lenses inside the imaging system.

Image distortion

Even when all the objects in the object plane are being imaged as clear images on the focal plane, distortion of the images can appear. Distortion means that the location of the objects on the image plane are not correct, leading to separations of the actual image points from the paraxially predicted locations on the image plane. This error consists in the different parts of the object being reproduced with different magnifications. At the left side of Figure 8.6 the distortion free image of a grid is shown, in case of paraxial imaging.

(a) Distortion free imaging
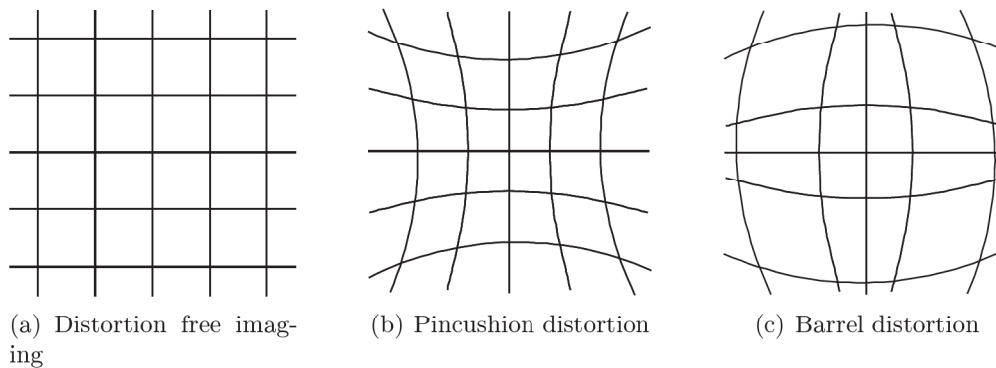
(b) Pincushion distortion

(c) Barrel distortion

Figure 8.6: Image distortion

When the magnification increases with the distance from the optical axis, a pincushion-shaped distortion appears, as is seen in Figure 8.6(b). However, when the magnification decreases with increasing distance, a Barrel distortion is the result, Figure 8.6(c). The resultant images are being imaged sharply onto the image plane, but distorted. Such distortions are the result of the use of apertures inside the imaging system. Furthermore, the amount of distortion depends on the distance between the aperture and the lens, i.e. a smaller distance leads to less distortion.

8.1.2 Chromatic optical aberrations

Chromatic aberrations occur when the imaging optics are used to transform the incident light, containing multiple wavelengths. It appears as a failure of the lens to focus all wavelengths onto the same point, as lenses have different refractive indices for different wavelength of the light (the so-called dispersion of the lens).

Figure 8.7 shows the result when polychromatic collimated light is incident on a positive lens. Because the index of refraction for shorter wavelengths is higher, these will be focussed closer to the optical system than larger wavelengths.
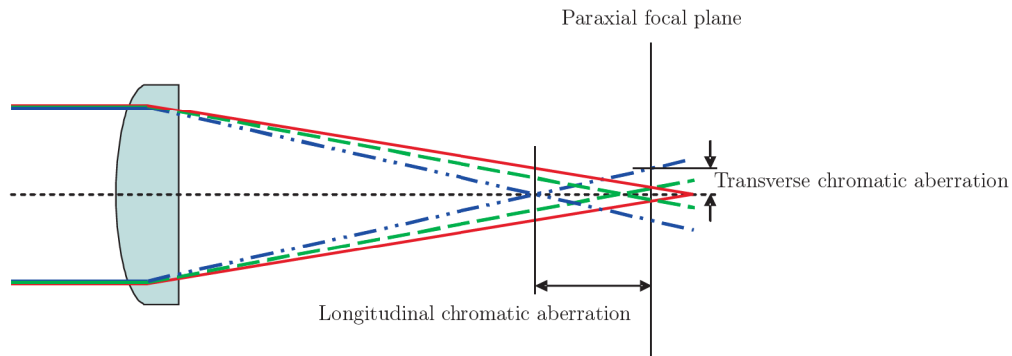

Figure 8.7: Principle of chromatic aberrations

Two kinds of chromatic aberrations can de defined: the longitudinal and the transverse aberrations. The longitudinal chromatic aberration is defined as the axial distance from the nearest to the farthest focal point. The transverse chromatic aberration is the occurrence of focussing of different wavelengths at different positions in the focal plane, as the magnification of the lens varies with the wavelength, i.e. blue light is refracted more than red light.

8.2 Optical imaging

The proposed volumetric particle image velocimetry measurement technique is aimed at capturing the three-dimensional, three-component velocity fields inside a volume at various heights. Two of the above described monochromatic aberrations are introduced in the proposed technique: astigmatism and the spherical lens aberration. Astigmatism is introduced by the dichroic filter, which is placed at an angle of 45° in order to divert the expanded laser beams through the measurement volume (Figure 6.10 in Chapter 3). As was explained in §(8.1), this means that rays, coming from the fluorescent tracer particles and passing through the dichroic filter in the meridional plane, travel another distance to the CCD chip of the camera than rays in the sagittal plane. As a result, the focal lengths in these two planes will be different, introducing a deformation of the particle in the image plane of the camera.

This image deformation depends on the thickness of the filter, t, the refraction index of the tilted filter, n, and on the angle of the tilted filter, θ. In Figure 8.8 the measurement volume depth is plotted as a function of the angle of the tilted filter and its thickness, according to eq. (8.3).

This figure shows clearly that for both increasing tilted angles and increasing thicknesses of the filter a larger volume measurement depth can be reached. In case a small depth of measurement is required, either the thickness of the filter has to be decreased, or the filter has
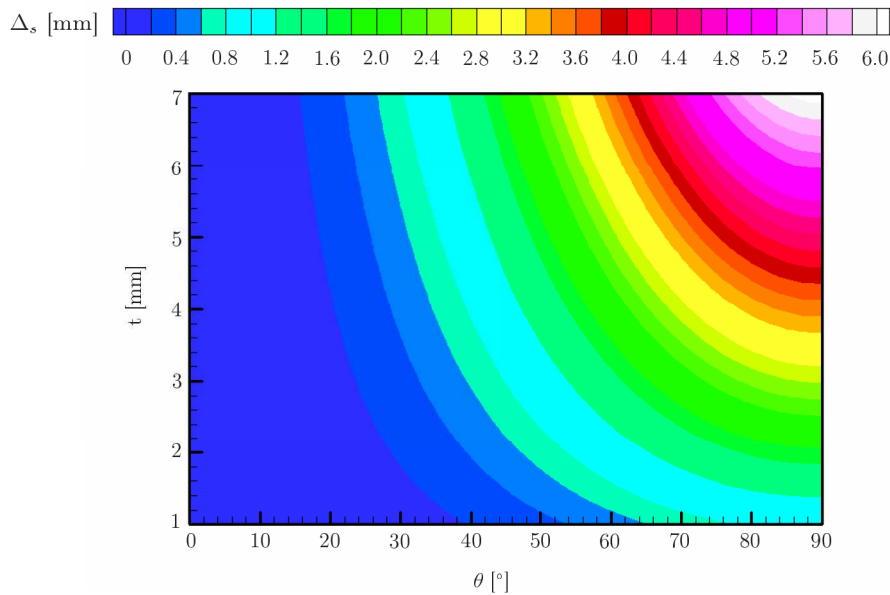
Figure 8.8: The dependence of the measurement volume depth on the angle θ and the thickness t of the dichroic filter ($n = 1.52$)

to be turned to smaller degrees of incidence.

In case of perfect astigmatism, particles will be imaged as horizontal or vertical lines at the focal planes, or as ellipses when the particles are located between these two focal planes. Due to the relatively low laser power, as the diameter of the laser beams is increased a factor four, and the long way the emitted light by the fluorescent tracer particles has to travel to the CCD chip of the camera, a small f-number is used in this measurement technique. This small f-number introduces the so-called spherical lens aberration, where rays which enter the lens far from the optical axis are focused more tightly than those that enter closer to the axis. As a result of the combination of these two monochromatic aberrations, tracer particles are imaged differently than in the case of perfect astigmatism.

Due to the astigmatism and spherical aberration of the optical system tracer particles located exactly at the focal lines of the sagittal or tangential plane are imaged respectively as vertical or horizontal ellipses, whereas particles in-between these two focal lines are imaged as stars of interchangeable major and minor axes. Eight exemplary images of two 10 μm RhodamineB fluorescent tracer particles are shown in Figure 8.9. The change in depth between the left and the right image is about 5 mm. In the upper left recording, the particles have ellipse-like shapes with a small vertical and a large horizontal main axis (Figure 8.9(a)). As the distance from the reference plane increases, these two axes decrease in length (Figure 8.9(b)) after which the horizontal focal plane is reached (Figure 8.9(c)). With further increase in distance between the reference and the image plane, the tracer particle images lie in-between the two focal planes, as a result of which star-shape images can be seen, having an interchangeable large and small main vertical and horizontal axis (Figure 8.9(d) and 8.9(e)). In Figure 8.9(f) the second focal plane (the vertical one) is reached, followed by growing ellipse-shaped particle images for larger distances (Figure 8.9(g) and 8.9(h)). The change of the shapes of these ellipses with the distance from the second focal plane is equal to those ellipses appearing before the first focal plane, only turned over an angle of 90°, as can be seen by comparing images (a) and (b) with, respectively, (h) and (g).
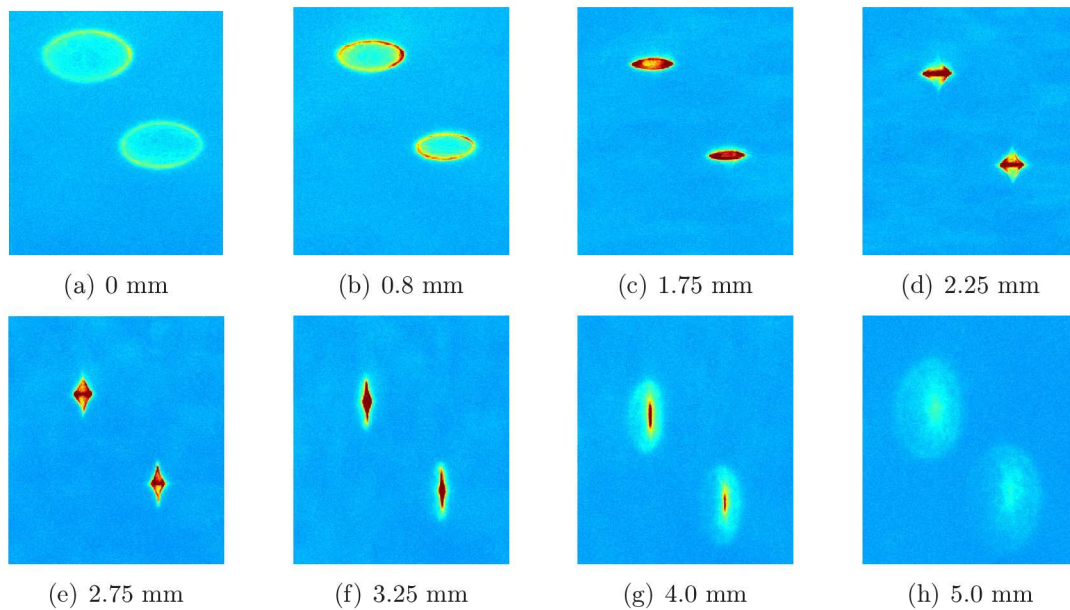
(a) 0 mm   (b) 0.8 mm   (c) 1.75 mm   (d) 2.25 mm

(e) 2.75 mm   (f) 3.25 mm   (g) 4.0 mm   (h) 5.0 mm

Figure 8.9: Chnage of the particle image shape with its position in the measurement volume (distances are measured from reference height at 0 mm)

8.3 Image data processing

This paragraph describes in detail the different image data processing subroutines, required to extract out of the recorded tracer particle images the velocity fields at different depths inside the measurement volume. Out of the recordings, the first step is to determine the number of particles per recording, their shape and position. This is mainly done by setting the right thresholds. Once the particles and their shapes are known, the central moments ratio of the intensity distribution is calculated for each particle and compared with the calibration curves to determine the three dimensional position of each particle inside the measurement volume. Due to the two applied monochromatic aberrations, the tracer particles are being imaged by a large area of pixels. This requires that the shapes of the particles are decreased, in order to be used for the velocity computation. The last step in the data processing is the computation of the velocity fields at different depths inside the volume. In order to do so, an averaging over several instantaneous recordings has to be done, to avoid too less particles per depth section.

8.3.1 Particle image reconstruction

The subroutine for analysing the shape, position and number of the tracer particle images is the most essential part of the pre-processing of the data for the proposed measurement technique, because the particle position in depth is directly linked to the particle image shape. In Figure 8.10, on the left hand side, an original particle image is shown.

After having recorded the particle images, a mean background intensity field is determined and subtracted. The threshold value is determined by analysing the intensity distributions of all images per recording. A mean intensity distribution over all the images is calculated, of which an histogram is made. The peak of this histogram, hence the intensity with the most entries, is set as the background intensity. Either this value of the intensity is taken directly as the threshold value, or, if necessary, a fraction of the difference between the maximum intensity

(a) Original particle image

(b) Segmentation after thresholding
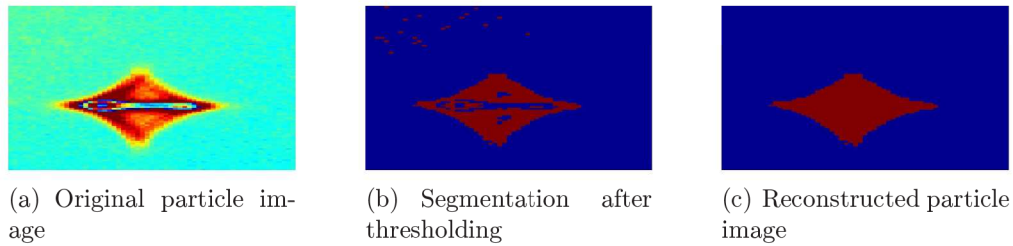
(c) Reconstructed particle image

Figure 8.10: Particle shape reconstruction from recorded tracer particle images

and the background intensity is added to increase the threshold with a few percent.

After background subtraction, two additional filters are applied, the first one to remove most of the remaining background noise, the second one to determine the pixels which might belong to the particle image (Figure 8.10(b)) by making use of a binarisation. As can be seen in this image, part of the background noise is still present. This noise is removed from the binary image by locating all connected objects that have less than a certain number of pixels and assigning them to the background. In the next step, the remaining pixels are connected to form a reconstructed particle image (Figure 8.10(c)). In this way, each image is scanned for all particles, a number is assigned to each particle and the exact shape is determined for the next step in the data processing.

8.3.2 Particle depth assignment through central moments ratio

The combination of astigmatism and the spherical lens aberration causes a wave front aberration which results in distorted particle images, as was explained in §(8.1.1). The emitted light intensity of each fluorescent tracer particle depends on the particle size, the position of the particle inside the measurement volume as well as on the laser beam quality and intensity. This emitted light intensity influences the width and height of each particle image. Therefore, a combination of the ratio between the horizontal and vertical 2nd order and 4th order central moments is chosen as a measure determining the particle depth position inside the measurement volume, since this ratio does almost not depend on the emitted light intensity of a particle.

In order to calibrate the imaging technique, dried RhodamineB tracer particles (diameter: 10 ± 0.19 μm PMMA particles; excitation wavelength 560 nm, emission wavelength 584 nm) are used, placed onto a plexiglass plate. This plate has the same thickness as the bottom of the plexiglass container, used for validation measurements afterwards, and is aligned orthogonally with the expanded laser beam and the long distance microscope. To simulate different three-dimensional positions of the particles in the measurement volume, the long distance microscope is translated horizontally along a total path of 5 mm with increments of 10 μm. At each step one image of the particles is taken. By scanning in this way the measurement volume, the change of the intensity distribution in the horizontal and vertical direction of the tracer particle images can be measured as a function of depth.

The depth of each tracer particle image is determined as follows. First of all the two-dimensional center of mass is determined by using the binary intensity distribution of the particle, $I(x, y)$, being a function of the coordinates x and y of the pixels belonging to the particle image:

$$x_c = \frac{\iint x I(x,y) dx dy}{\iint I(x,y) dx dy} \tag{8.6}$$

$$y_c = \frac{\iint y I(x,y) dx dy}{\iint I(x,y) dx dy} \tag{8.7}$$

With the use of the coordinates of the center of mass of the particle, the 2nd and 4th order central moments of the intensity distribution can be calculated

$$\mu_{2x} = \iint (x - x_c)^2 I(x,y) dx dy \tag{8.8}$$

$$\mu_{2y} = \iint (y - y_c)^2 I(x,y) dx dy \tag{8.9}$$

$$\mu_{4x} = \iint (x - x_c)^4 I(x,y) dx dy \tag{8.10}$$

$$\mu_{4y} = \iint (y - y_c)^4 I(x,y) dx dy \tag{8.11}$$

In Figure 8.11 the 2nd and 4th order central moments of the intensity distribution of each tracer particle image are plotted versus the depth.

These figures show that the 2nd and 4th order central moments have the same shape, but the magnitude of the values are different. It is noticed that the vertical central moments are perfectly symmetrical with respect to the mid-point in the depth scanning direction (here 2000 μm), whereas the minimum for the horizontal central moments is shifted to higher values of the depth. The equations of the fitted curves for the left and right parts of the lines are given in Table 8.1.

Table 8.1: Equations for the fitted linear curves of the 2nd and 4th order central moments of the particle image intensity distributions

Central moment	Part	Equation
μ_{2x}	Left	$\log(\mu_{2x}) = -9.4 \cdot 10^{-4} \ d + 6.7818$
	Right	$\log(\mu_{2x}) = 11.1 \cdot 10^{-4} \ d + 0.1689$
μ_{2y}	Left	$\log(\mu_{2y}) = -12 \cdot 10^{-4} \ d + 6.3846$
	Right	$\log(\mu_{2y}) = 10.2 \cdot 10^{-4} \ d + 1.9290$
μ_{4x}	Left	$\log(\mu_{4x}) = -14.8 \cdot 10^{-4} \ d + 10.2129$
	Right	$\log(\mu_{4x}) = 19.4 \cdot 10^{-4} \ d - 1.1042$
μ_{4y}	Left	$\log(\mu_{4y}) = -19.3 \cdot 10^{-4} \ d + 9.3460$
	Right	$\log(\mu_{4y}) = 17.8 \cdot 10^{-4} \ d + 2.2079$

By using these equations, each particle in the measurement volume has its unique combination of the magnitude of the horizontal and vertical central moments, out of which the unique central moment ratio can be calculated and used for the determination of the exact position of the particle in space.
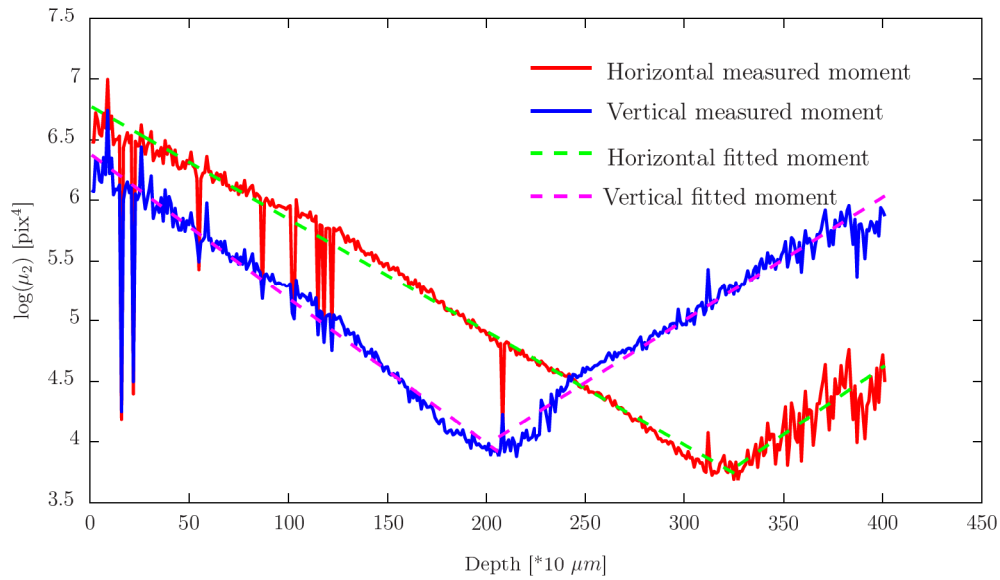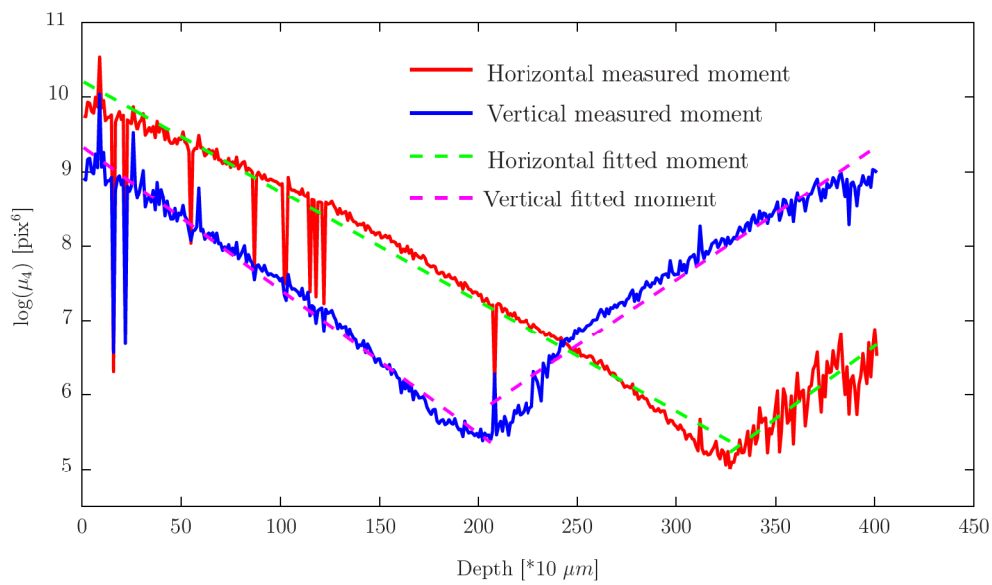
(a) 2nd order central moment

(b) 4th order central moment

Figure 8.11: Change of 2nd and 4th order central moments of the intensity as a function of the depth inside the measurement volume for a 10 μm RhodamineB particle

This ratio of the two central moments of each particle image is now obtained by the following equation

$$\mu = \frac{\mu_2 + \mu_4}{2} \tag{8.12}$$

Here, μ_2 and μ_4 are defined respectively as

$$\mu_2 = \left[\frac{\mu_{2x}}{\mu_{2y}}\right]^{1/2} \tag{8.13}$$

$$\mu_4 = \left[\frac{\mu_{4x}}{\mu_{4y}}\right]^{1/4} \tag{8.14}$$

When the central moments ratio for each particle image is calculated with the equations mentioned above, the calibration curve, given in Figure 8.12, is received.
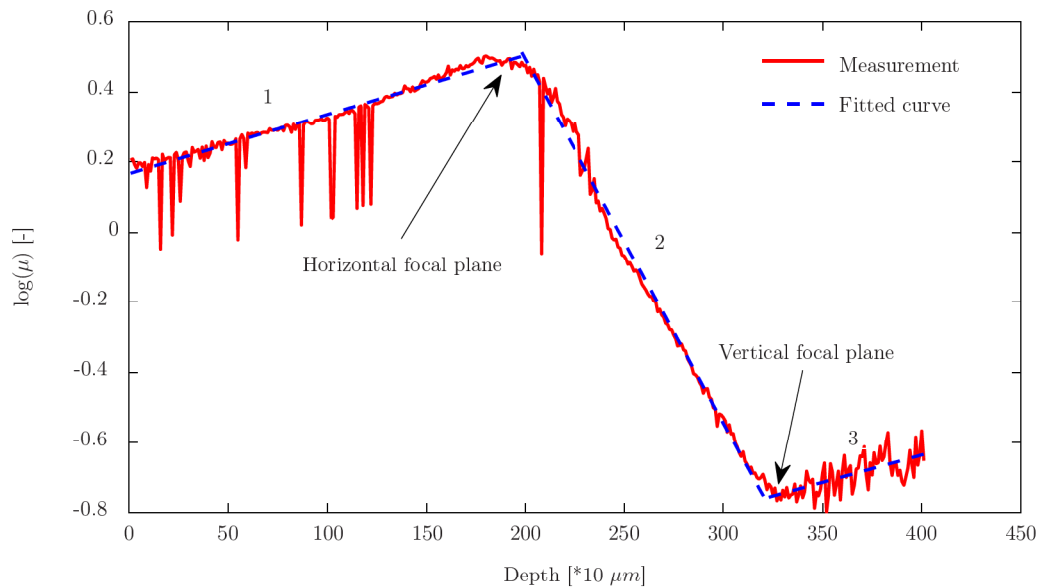

Figure 8.12: Change of the central moments ratio of the intensity as a function of the depth inside the measurement volume for a 10 μm RhodamineB particle

It can be seen in this figure that the curve consists of three linear parts, denoted 1 to 3. Part 1 corresponds to the depths where the particle images are ellipses extended in the horizontal direction (Figure 8.9(a) and 8.9(b)), and part 3 to the depths where the particles are observed as ellipses extended in the vertical direction (Figure 8.9(g) and 8.9(h)). Both curves have the same slope, i.e. the same change in central moments ratio, because the particles are imaged in the same way. Part 2 of the calibration curve corresponds to the particles which are observed as star-like images (Figure 8.9(d) and 8.9(e)). The equations of the fitted curves for the three linear parts of the calibration curve are shown in Table 8.2. The distance between the maximum and the minimum value of part 2 (highlighted by arrows in Figure 8.12) is the astigmatic difference between the two focal planes, Δ_s, and has a value of about 1.3 mm. This value is close to the theoretical value, calculated by eq. (8.3), of 1.1 mm for the dichroic filter

used ($t = 4.1$ mm, $\theta = 45°$ and $n = 1.52$). By a change of 1 pixel in one of the main axes' lengths, the central moments ratio changes by an amount of $5 \cdot 10^2$, resulting in a theoretical depth resolution of 131 μm in part 1 and 3, and of 14 μm in part 2.

Table 8.2: Equations for the fitted linear curves of the central moments ratios of the particle image intensity distributions

Central moment	Part	Equation
μ	1	$\log(\mu) = 1.7 \cdot 10^{-4} \ d + 0.1655$
	2	$\log(\mu) = \text{-}10.4 \cdot 10^{-4} \ d + 2.5645$
	3	$\log(\mu) = 1.6 \cdot 10^{-4} \ d \text{ - } 1.2640$

In order to assure repeatability of this curve, six independent calibration measurements were done. For each measurement the whole imaging system, i.e. laser source, plexiglass plate and camera, was readjusted to assure the best possible quality of the tracer particle images. Nonetheless, this led to slightly different intensities of the laser beams as well as different imaging angles of the camera, as the settings of the previous measurement could never be regained in a perfect way. Figure 8.13 shows the central moments ratios for these six recordings.
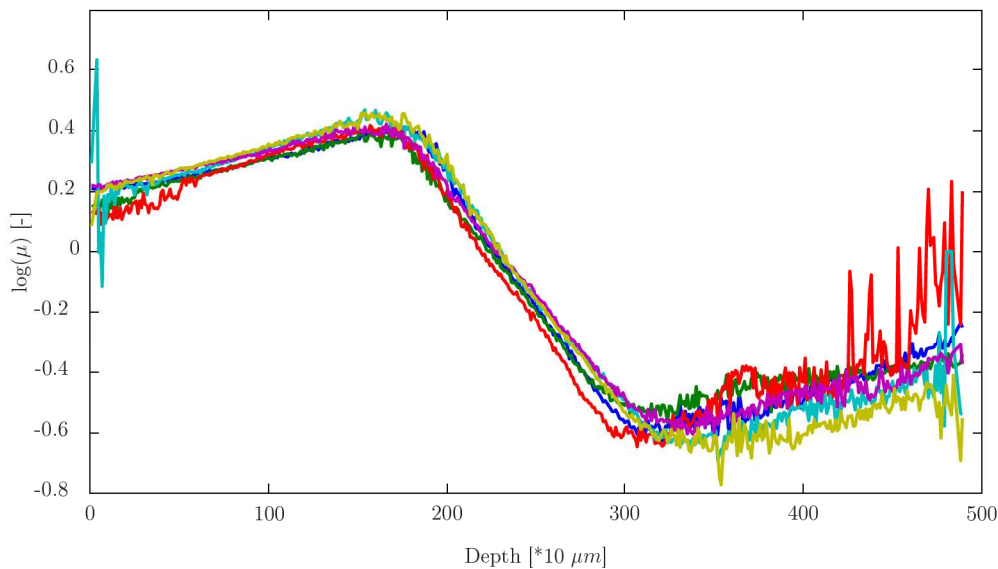

Figure 8.13: Change of the central moments ratio of the intensity as a function of the depth inside the measurement volume for six different 10 μm RhodamineB particles

These curves show a clear scattering of the data between the different calibrations. In order to investigate this scattering, Figure 8.14 and Figure 8.15 show the statistical distributions, i.e. mean and standard deviation, of respectively the central moments ratio and the depth.

The first figure shows the distribution of the mean of the six central moments ratios, as well as the range formed with the standard deviation between which 68% of the central moments
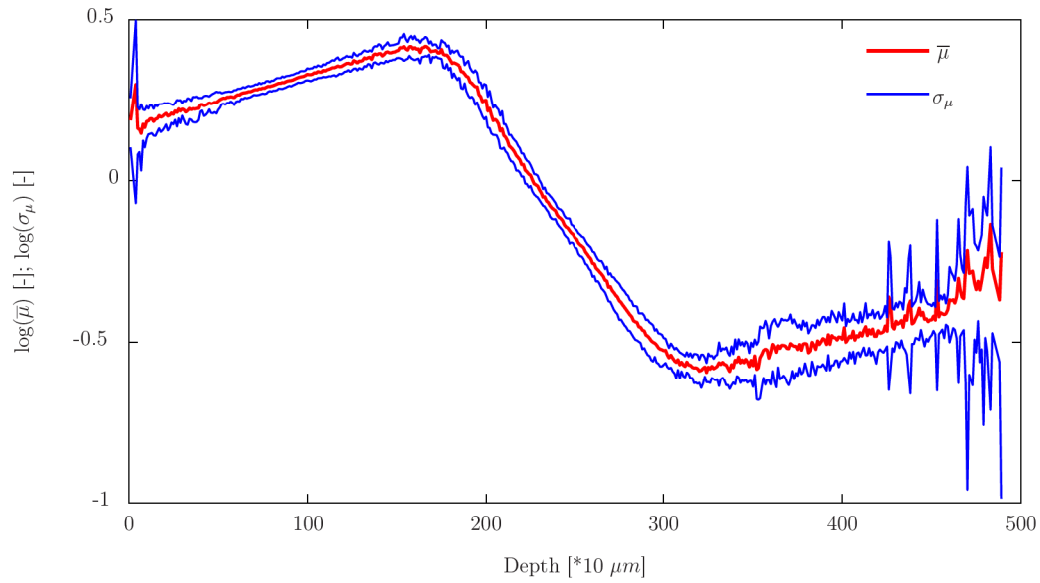
Figure 8.14: Distribution of the mean and standard deviation of the central moments ratio of the intensity as a function of the depth inside the measurement volume for six different 10 μm RhodamineB particles
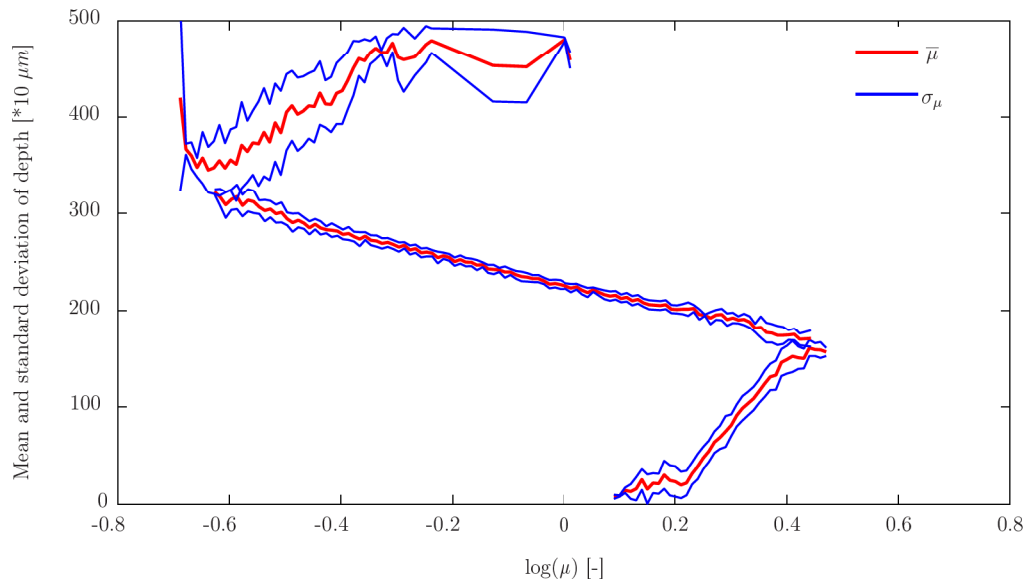

Figure 8.15: Distribution of the depth inside the measurement volume as a function of the central moments ratio of the intensity for six different 10 μm RhodamineB particles

ratios can be found, both as a function of the depth inside the measurement volume. The standard deviations for the first two parts of the curve, i.e. between 0 μm and 3180 μm are found to be very small, being 2.3% and 3.9%, whereas for the last part of the curve, from 3180 μm on, the standard deviation increases to 9.1%. This increase results from the background noise, which becomes more important in this depth range, thereby introducing errors in choosing the right threshold for the particle shape recognition and following data analysis.

The second figure shows the range of depths for each mean of the six central moments ratios; hence, the error which is being made by defining to each μ a certain depth inside the measurement volume. It is seen that only for the upper part of the curve, i.e. for large values of the depth, a large range of possible depths can be defined for each μ, therefore introducing large errors in the analysis of the data. In this region the standard deviation lies around 280 μm, whereas for the middle and lower part of the curve, these values are respectively 11 μm and 8 μm.

To assure a well defined depth for each μ, it is therefore necessary to obtain a calibration of the central moments ratio through the measurement volume before each velocity measurement. This makes this measurement technique, however, time-consuming, in case no automatic scanning procedure is being used.

8.3.3 Transformation of the particle shape for computation of velocity fields

After each particle in every recording has been assigned a number and its three-dimensional position inside the measurement volume has been determined, a square segment of the image, which contains the particle image, is extracted. To change the large distorted particle images into small spherical particle images useable for the computation of the velocity fields, the data processing algorithms for the separation of anamorphic images described by Angarita-Jaimes *et al* [2] are applied. They proposed two different algorithms: the spherical averaging and the spherical blending. The principles of these algorithms are shown in Figure 8.16.

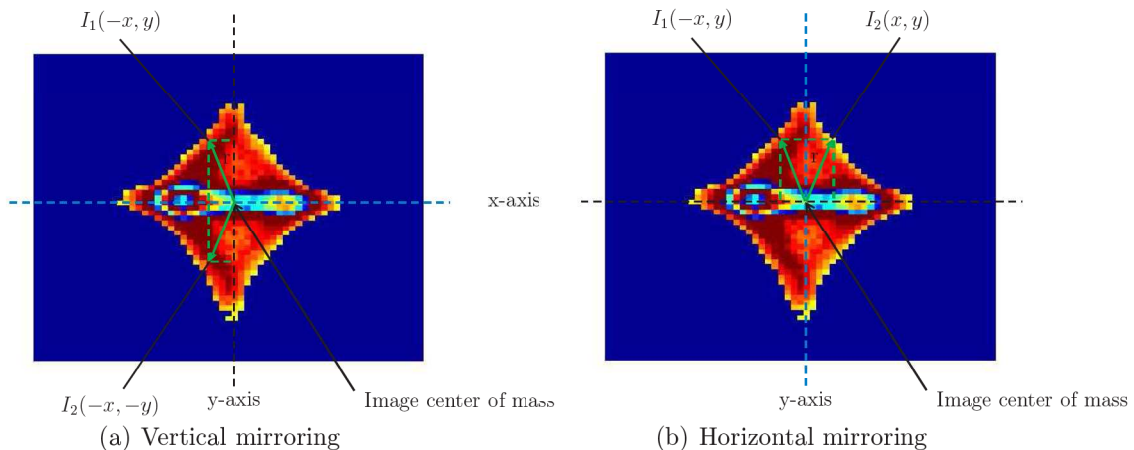(a) Vertical mirroring   (b) Horizontal mirroring

Figure 8.16: Principle of spherical averaging and blending to transform the distorted particle images to spherical images

The first approach is based on generating two averaged particle images, once by averaging the intensities in the vertical direction (Figure 8.16(a)) and once in the horizontal direction (Fig-

ure 8.16(b)). For the vertical averaging method each pixel of tracer particle, which lies above the horizontal axis going through the center of mass, is being scanned, for example $I_1(-x, y)$ in Figure 8.16(a). At this scanned pixel the position of the pixel is mirrored in the horizontal axis ($I_1(-x, -y)$ in Figure 8.16(a)), after which the mean of the intensities of these two pixels is calculated. This mean intensity is then substituted at the two pixel positions. This is done for each pixel positioned above the horizontal axis, as a result of which a new tracer particle image appears, having the same intensity distribution above and below the horizontal central axis. The same approach is applied for the horizontal averaging method, but now the images at the left of the vertical central axis are mirrored with those on the right (Figure 8.16(b)), in order to get a new tracer particle image, but with the same intensity distribution at the left and at the right of the vertical axis. The final spherical tracer particle image is obtained by adding the intensity distributions of these two images together. In this way, a spherical particle image is obtained with concentric rings, centered around the center of mass, of which each pixel, belonging to the same concentric ring, has the same intensity.

The second approach - spherical blending - described by Angarita-Jaimes *et al* [2], is also based on obtaining two averaged particle images, but without losing the intensity distribution of the original particle image. Here, a one-dimensional integration of the intensity field of the particle image is performed, which means that the two-dimensional image is projected onto each of its main axes going through the center of mass of the particle image. Just like for the spherical averaging algorithm these projections are then used to produce new two-dimensional particle images, by rotating the projections about the particle's center of mass, in this way producing an x-image and a y-image, as is seen in Figure 8.17.
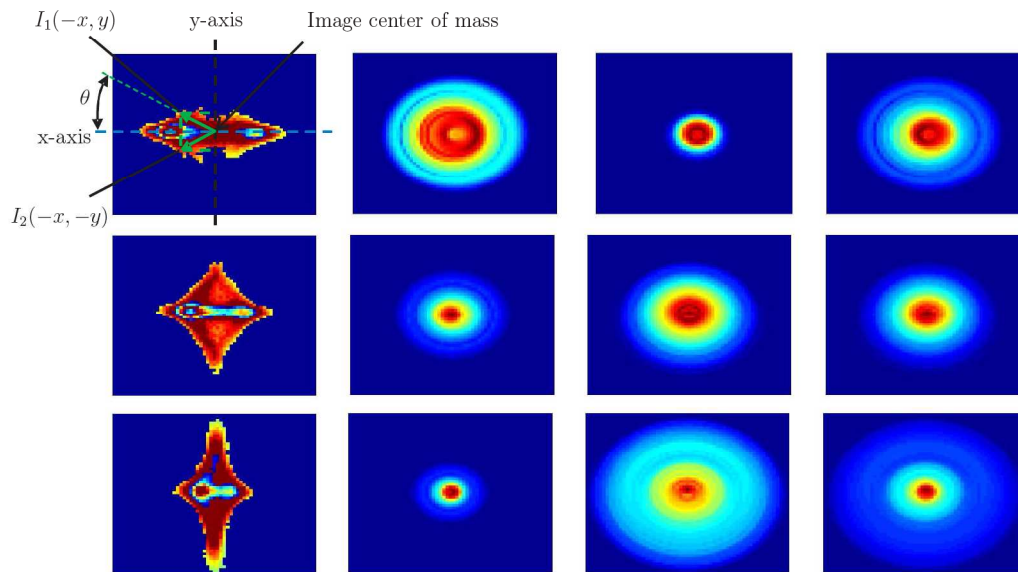
Figure 8.17: Principle of spherical blending. Left column: the original anamorphic images of the tracer particle images at different depth positions inside the measurement volume; middle columns: the extracted x-images and y-images; right column: the combined new particle images. All images are 61×61 pixels

The three images on the left show the original recorded distorted particle images, whereas the images in the middle are the x-images and y-images after projection. The asymmetry in

intensity between the left and the right side of the original particle images with respect to its center of mass is maintained by using a weighting factor. This means for the x-array, that each pixel in the synthesized image has a weighted intensity value by using weighted and interpolated intensity data from the left and right side of the x-array relative to the center position. The same is done for the y-array, by weighting and interpolating the upper and lower side of the y-array. These weighting functions are given by the following equations for the x-images and y-images respectively:

$$I_x(x,y) = I_{x,1}(x,y) \cdot \left(1 - 0.5\big(1 + \cos(\theta)\big)\right) + I_{x,2}(-x,y) \cdot 0.5\big(1 + \cos(\theta)\big) \qquad (8.15)$$

$$I_y(x,y) = I_{x,1}(x,y) \cdot \left(1 - 0.5\big(1 + \cos(\theta - 0.5\pi)\big)\right) + I_{x,2}(x,-y) \cdot 0.5\big(1 + \cos(\theta - 0.5\pi)\big) \quad (8.16)$$

The synthesized particle images are created by adding the extracted intensity distributions of the x-images and y-images together, in this way obtaining the final spherical particle images with preservation of the original intensity distributions for each tracer particle.

For this measurement technique the second method based on the spherical blending algorithm is used, as the intensity distributions for each particle image can be used for sub-pixel particle displacement calculations. As can be seen in Figure 8.17 the size of the tracer particle images can become quite large, i.e. several tens of pixels, which will give difficulties in the determination of the velocity distribution, as will be explained in the next paragraph. To overcome these problems, the particle images are all decreased in size to 9×9 pixel particle images, preserving the intensity distributions of each image. These new spherical images are subsequently placed with their centers of mass onto the centers of mass of the original distorted particle images. In this way, all the distorted particles in each recording are changed into spherical particles having a diameter of nine pixels, each of them having the same intensity distribution as the original particle images.

8.3.4 Computation of velocity fields

The proposed technique is developed as a three-dimensional, three-component velocity measurement technique. However, in this thesis the computations and the presentations of the velocity fields are described only by using a three-dimensional, two-component multi-layer data processing algorithm.

In §(8.3.2) the algorithm which assigns to each of the particles in the recorded images a depth inside the measurement volume, has been presented. To compute the velocity fields at different depths, the measurement volume is split up into different layers depending on the axes ratio range obtained by the calibration of the measurement volume. For each of these layers all images are scanned, during which only these particle images are taken which fall inside this depth range and deleting all the other particles. In this way, new pairs of particle images are generated with a low density of seeding particles. Due to the low particle density the number of signals is not enough to obtain valid velocity vectors from the instantaneous cross-correlation functions in the PIV-processing algorithm, which can then potentially lead to erroneous velocity vectors in each instantaneous vector field. For standard PIV algorithms these erroneous vectors are normally identified and removed by interpolation of the neighbouring vectors (Westerweel [189], Meinhart *et al.* [94]), but due to the low signal of the present

recordings, this interpolation does not result in satisfactory instantaneous and mean vector fields.

To overcome this problem, a modified version of the *WIDIM* PIV-algorithm (Scarano [146]), based on a window-deformation and iterative multi-grid cross-correlation, is applied. First, instantaneous averaged recordings are produced by adding twenty new pairs of particle images together to assure that there are enough particle image pairs for most of the interrogation areas to obtain a clear signal-to-noise ratio and a correct correlation peak identification. The number of particle recordings per averaged recording is fixed at twenty to avoid an overlapping of the single particles and thereby reducing the signal-to-noise ratio, as for overlapping particles no clear lengths of the two main axes can be obtained for each of these particles, due to which all of them have to be discarded. However, even after averaging over multiple images, there appear still interrogation areas inside the images with low signal-to-noise ratios, therefore introducing relatively high errors in the velocity measurements and resulting in outliers in the mean velocity field and in the standard deviations. This can be canceled by making use of the average correlation method described by Meinhart *et al.* [96]. For each instantaneous averaged recording the cross-correlation functions are calculated, after which the cross-correlation fields of all averaged recordings are added together to produce an averaged correlation field, out of which the locations of the signal peaks are determined. Hence, all the interrogation areas having low signal-to-noise ratios contribute only little to the average correlation function, whereas high signal-to-noise ratios produce a much higher signal peak. This averaged vector field is then used for the next iteration step inside the PIV-algorithm. In this way, the probability of erroneous vectors in the mean velocity field is greatly reduced.

To validate the subroutine that calculates the velocity fields using the average correlation method, two different sets of *synthetic* PIV images are used: a uni-directional two-dimensional translation flow and a solid body rotational flow. The two-dimensional translation flow has a uniform particle translation given by the following equations:

$$u_{trans,x} = 10 \quad pix$$

$$u_{trans,y} = 5 \quad pix \tag{8.17}$$

resulting in a translation magnitude of $u_{trans} = \sqrt{125}$ pix. The solid body rotational flow consists of a uniform rotational flow of $\Omega = 5 \cdot 10^{-3}$ rad, resulting in a velocity field given by

$$u_{vortex} = 2\pi\Omega R \quad pix \tag{8.18}$$

In this equation, R is defined as

$$R = \left((x - x_0)^2 + (y - y_0)^2\right)^{0.5} \quad pix \tag{8.19}$$

with (x_0, y_0) being the coordinates of the center.

After having chosen a certain depth range for the investigation of the velocity field inside the measurement volume, all the particle images which have a value of μ that lies outside the investigated range are being deleted in the recordings. As has been described above, this results in new recordings with relatively low seeding densities. To assure enough particle image pairs for most of the interrogation areas of the recordings, in order to obtain a clear signal-to-noise ratio and a correct correlation peak identification, the so-called instantaneous averaged recordings are produced by adding twenty new pairs of particle images together. To investigate

whether there exists an influence of this particle density on the outcome of the subroutine, five different seeding densities are generated for the synthetic recordings, in the range of 125 to 2000 synthetic particles per image.

In Figure 8.18 the mean velocity fields are shown over 150 images for both the uniform translational flow (left column) and the uniform solid body rotational flow (right column) for three different tracer particle seeding densities, namely 125, 500 and 2000 particles per image. It is being referred to Appendix E for the mean velocity fields of both flows for the other two investigated seeding densities of 250 and 1000 tracer particles per image.

For all investigated seeding densities it can be seen that the mean velocity distribution, both in direction and magnitude, is being calculated correctly by the velocity computation algorithm of the PIV processing toolbox. However, some minor differences can be seen for both flows for increasing seeding density. For the uniform translational flow it is seen that for the lowest seeding density, here 125 particles per image, the magnitude of the velocities is uniform around $\overline{U}_{tot} = \sqrt{125} \approx 11.18$ pix/s with slightly higher values at the right side of the image due to particles leaving the image, resulting in particle pair losses and slightly higher calculated velocities. As the seeding density is increased, there appear small areas with higher total mean velocities up to values of $\overline{U}_{tot} = 12.3$ pix/s, Figure E.1(a) and 8.18(c). The higher the seeding density gets, the larger these areas become, having larger parts reaching the maximum mean calculated velocity of $\overline{U}_{tot} - 12.3$ pix/s, compare Figure 8.18(a) with Figure 8.18(e). However, for the investigated solid body rotational flow it is found that by increasing the seeding density, the calculated velocity field is almost not influenced. There are some minor changes in the local velocity magnitudes, but the overall expected rotational velocity field is achieved very well. Only for the seeding density of 125 pixels per image, Figure 8.18(b), it is found that the circular velocity field is not being calculated correctly at several positions.

As both input flows are completely uniform, without any disturbances, these small changes in the mean velocity magnitude for both flows are being introduced by the velocity computation algorithm itself. As was mentioned already above, this is the result of the loss of particle pairs inside an interrogation area between image A and image B, Figure 6.8. Due to the loss of particle pairs a wrong cross-correlation peak is calculated for this interrogation area by the inverse Fourier Transform algorithm, resulting in a wrong displacement vector, thereby influencing the mean velocity at this interrogation area. Due to the possible loss of particle pairs, resulting in these small fluctuations in velocity magnitude and direction between the 150 image pairs, artificial fluctuations in the velocity, hence turbulence, is being introduced by the algorithm. The turbulence intensity distributions, calculated by eq. (6.17), are given for both flows (the uniform translational flow (left column) and the uniform solid body rotational flow (right column)) for three different tracer particle seeding densities of 125, 500 and 2000 particles per image in Figure 8.19. It is again being referred to Appendix E for the turbulence intensity distributions of both flows for the other two investigated seeding densities of 250 and 1000 tracer particles per image.

For the uniform translational flow with 125 particles per image, it is found that an artificial turbulence intensity between 1% and 6% is being introduced by the velocity computation algorithm. This artificial turbulence is distributed randomly, as is to be expected for a uniform translational flow. When the seeding density in the images is increased, there appear small areas with higher total mean velocities, which increase in size with increasing particle density, as has been described above. It can be seen in Figure E.5(a) and Figure 8.19(c) that for increasing particle densities, the turbulence intensity starts to decrease, but that, however, at the areas
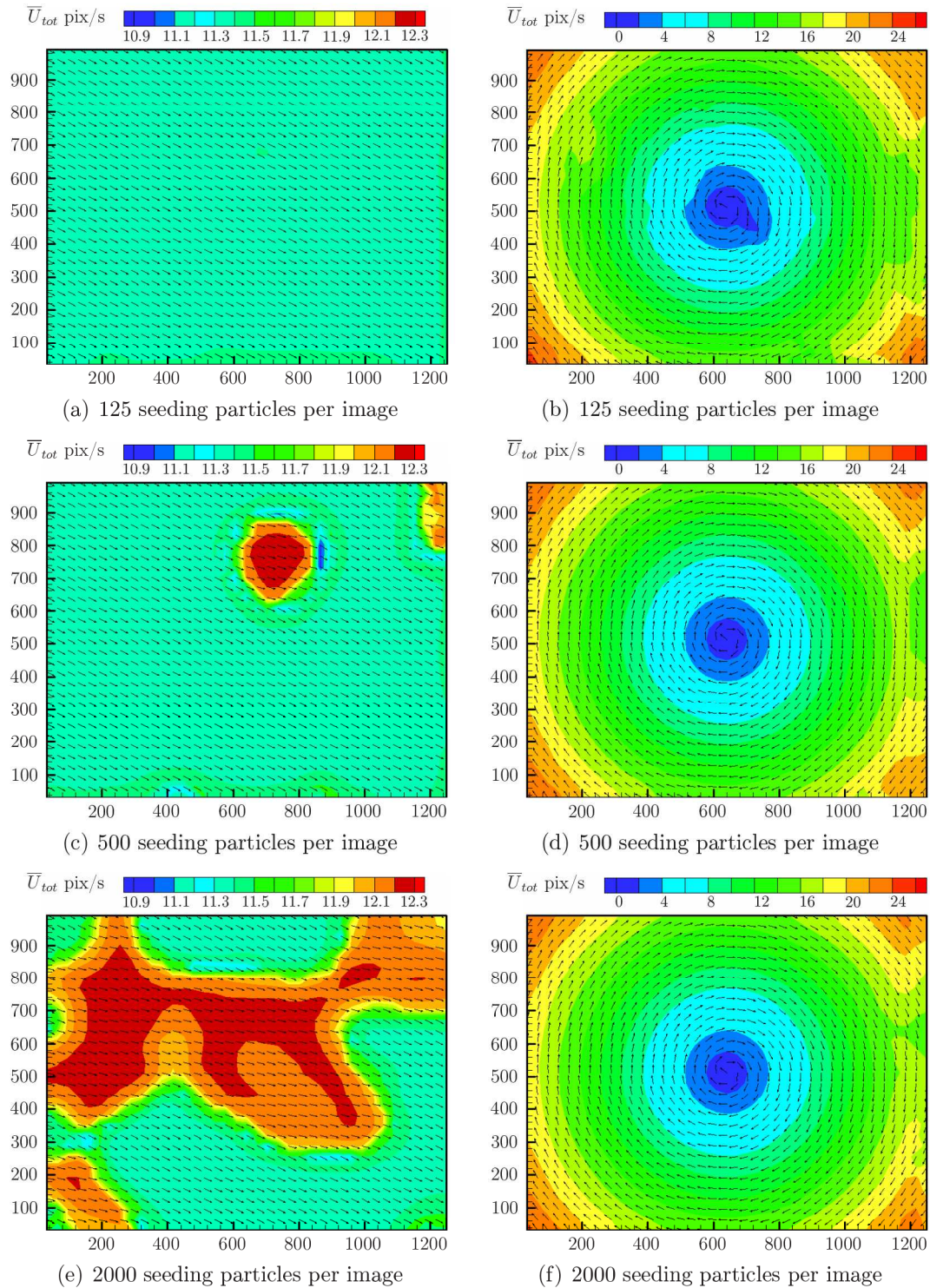
(a) 125 seeding particles per image

(b) 125 seeding particles per image

(c) 500 seeding particles per image

(d) 500 seeding particles per image

(e) 2000 seeding particles per image

(f) 2000 seeding particles per image

Figure 8.18: Mean velocity field for a uniform translational input flow of $\overline{U}_{tot} - \sqrt{125}$ (left) and a uniform solid body rotational flow of $\overline{U}_{tot} = 3.1416 \cdot 10^{-2} R$ (right) for three different seedings densities of 125, 500 and 2000 tracer particles per image

(a) 125 seeding particles per image

(b) 125 seeding particles per image

(c) 500 seeding particles per image

(d) 500 seeding particles per image

(e) 2000 seeding particles per image
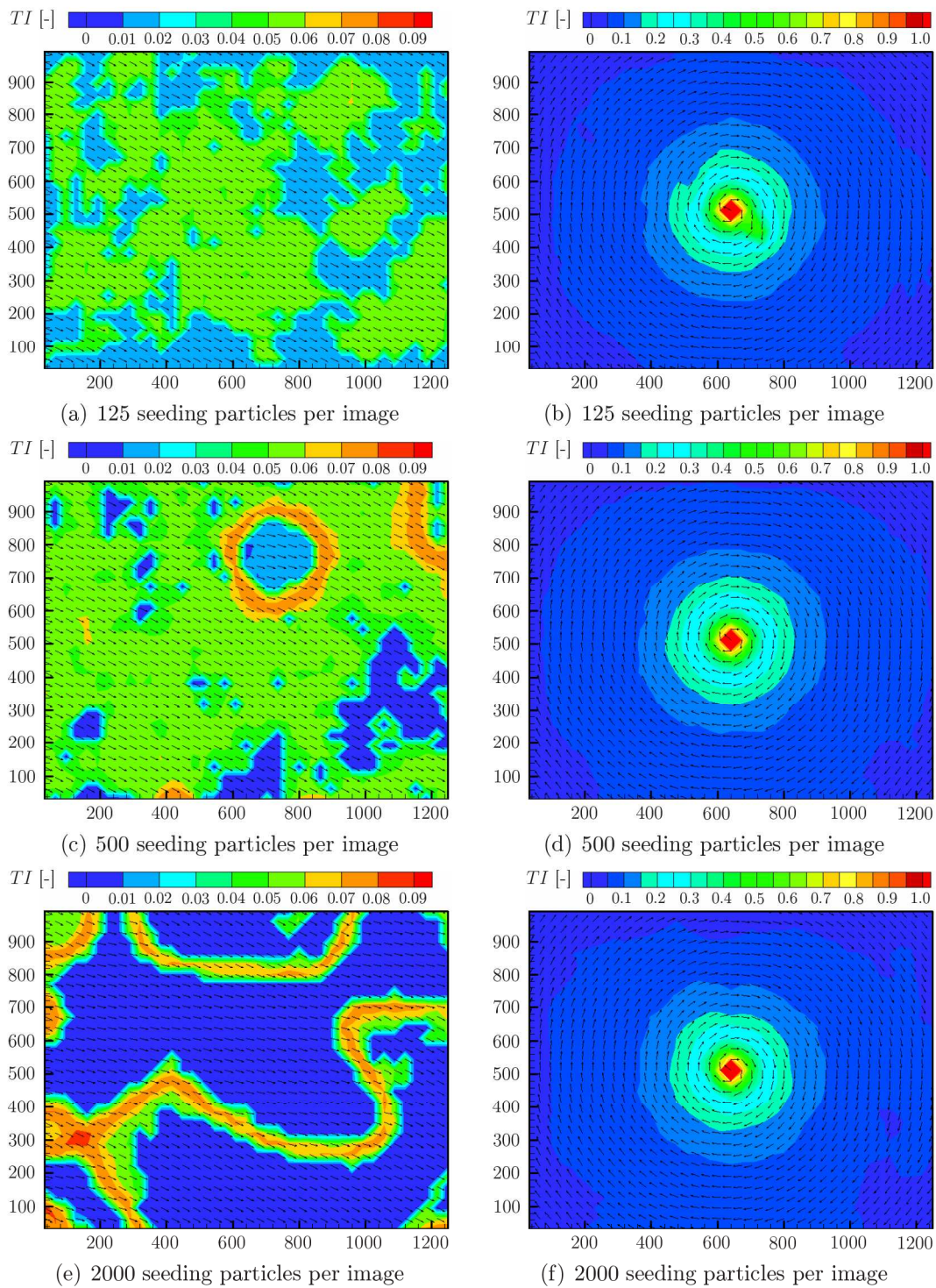
(f) 2000 seeding particles per image

Figure 8.19: Distributions of the turbulence intensity for a uniform translational input flow of $\overline{U}_{tot} = \sqrt{125}$ (left) and a uniform solid body rotational flow of $\overline{U}_{tot} = 3.1416 \cdot 10^{-2}R$ (right) for three different seedings densities of 125, 500 and 2000 tracer particles per image

where higher mean velocities are calculated, the turbulence intensity increases up to 9%. The higher the seeding density gets, the lower the overall artificial turbulence intensity is, i.e. in the range of 0% and 1%, but the more areas appear where the turbulence intensity increases up to a maximum of 9%, Figure 8.19(e). These areas with higher turbulence intensities are found at the complete edge of the areas with higher mean velocities, which is to be expected, as here the mean velocity magnitude change is the highest, therefore introducing more velocity fluctuations between the recordings. These velocity fluctuations are present in both directions, hence horizontal and vertical, and are presented in Appendix E. It can be seen in Figure E.2 and Figure E.3 that the velocity fluctuations in both directions are about the same in magnitude, therefore contributing equally to the turbulence intensity.

The artificially generated turbulence intensity for the solid body rotational flow is found to be independent of the seeding density and lies between 0% and 100%, see the right side of Figure 8.19. It is found that the more the center of the rotational body is approached in radial direction, the higher the turbulence intensity gets, up to a maximum value of 100% at exactly the rotation center. Just as for the uniform translational flow it is found that the velocity fluctuations in both directions are about the same in magnitude, therefore contributing equally to the turbulence intensity, as is seen in Figure E.7 and Figure E.8.

It can therefore be concluded that the velocity computation algorithm, used to obtain the mean velocity fields and its fluctuations at different depths inside the investigated measurement volume, introduces by itself already artificial velocity fluctuations. Although these velocity fluctuations are mostly lying below 9%, they must be taken into account when calculating the velocity fields obtained by the validation measurements described in the next paragraph, in order to avoid large errors in the interpretation of the calculated turbulence intensity fields.

8.4   Validation measurements

To validate the proposed measurement technique, a laminar flow between two disks having a diameter of 300 mm, of which the upper one is rotating with a constant frequency, is used. A simplified schematic of the experimental setup is shown in Figure 8.20. The optical setup is based on the common micro-PIV setup, as has been described in §(6.2.2) for the measurements of the radial film velocity fields for spray impingement. The laser pulses of a Spectron Dual SL404 Twin pulsed Nd:YAG laser (532 nm, 100 mJ/pulse) are expanded in diameter up to a diameter of about 12 mm using a Keplerian beam expander. A dichroic filter, placed under 45° and having a maximum reflection in the bandwidth of 535 nm ± 15 nm, diverts the expanded laser beams upwards where they pass the investigated flow. In this way, a vertical cylindrical volume illumination of 12 mm in diameter is created.

The part of the setup, containing the investigated flow, consists of a round container of plexiglass, having a diameter of 300 mm and holding a glycerine/water mixture (70 Vol%-30 Vol% respectively) in which 10 μm RhodamineB PMMA particles have been suspended. The top of the liquid is covered with a plexiglass plate, connected to a viscometer. A viscometer is used, as it can rotate with low revolutions per minute. As the viscometer rotates with a constant frequency, a laminar flow is created, used for validation of the proposed technique, as this flow field can be described theoretically and numerically in an easy way. The exact vertical position of the covering plate is observed using a PCO CCD Sensicam camera (1280 × 1024 pix, 12 bit) in order to determine the exact height of the liquid film. This camera is fitted with an extended 50 mm focal length Nikkor lens from Nikon and used in single image mode as a
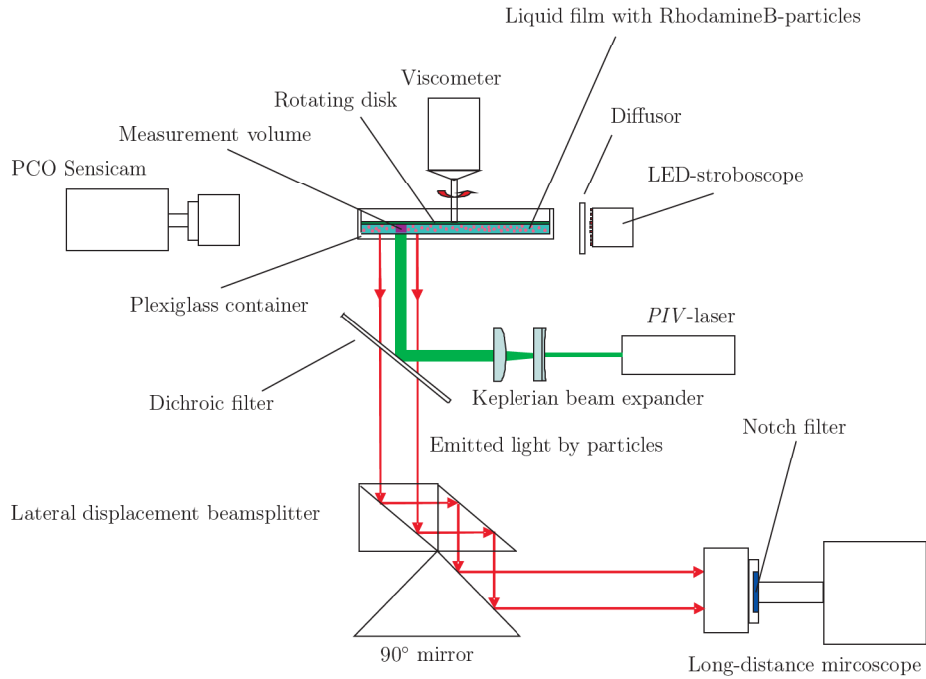
Figure 8.20: Layout of the two-dimensional laminar flow for the validation of the volumetric *PIV*-technique

detector. For this camera the exposure time is set to 10 μs and the field of view is 10.7 × 8.5 mm, hence a spatial resolution of 8.3 $\mu m/pix$ is present.

The light emitted by the particles passes through the dichroic filter and a lateral displacement beamsplitter, after which it is recorded by a second PCO CCD Sensicam camera. This camera is equipped with a long distance microscope (Nikon Nikkor 105 mm lens together with a 160 mm extension tube) and a notch filter. The notch filter has a transmission in-between 539 and 1200 nm, thus filtering out most of the green laser light reflections. The field of view of this camera is 5.6 mm × 4.5 mm with a spatial resolution of 4.4 $\mu m/pix$.

The recorded measurement volume has dimensions of 5.6 × 4.5 × 2.1 mm and is positioned at a distance of 99 mm from the rotating axis. The maximum out-of-plane theoretical spatial resolution is 131 μm, as was derived in §(8.3.2). The upper disk rotates with a constant frequency of 0.83 Hz, resulting in a maximum azimuthal velocity in the measurement volume of 516 mm/s. The mean radial velocity profile of the liquid at a height z inside the measurement volume can be well approximated by:

$$\overset{4}{} \quad u_\phi = \frac{r\Omega z}{h} \tag{8.20}$$

The two-dimensional equation can be used, since the radial coordinate r of the illuminated volume is much larger than the liquid film thickness h. In this equation the vertical coordinate z equals 0 mm at the bottom of the liquid layer and 2.1 mm at the surface of the rotating disk.

---

[4]Spurk [160]

(a) Analytical calculation
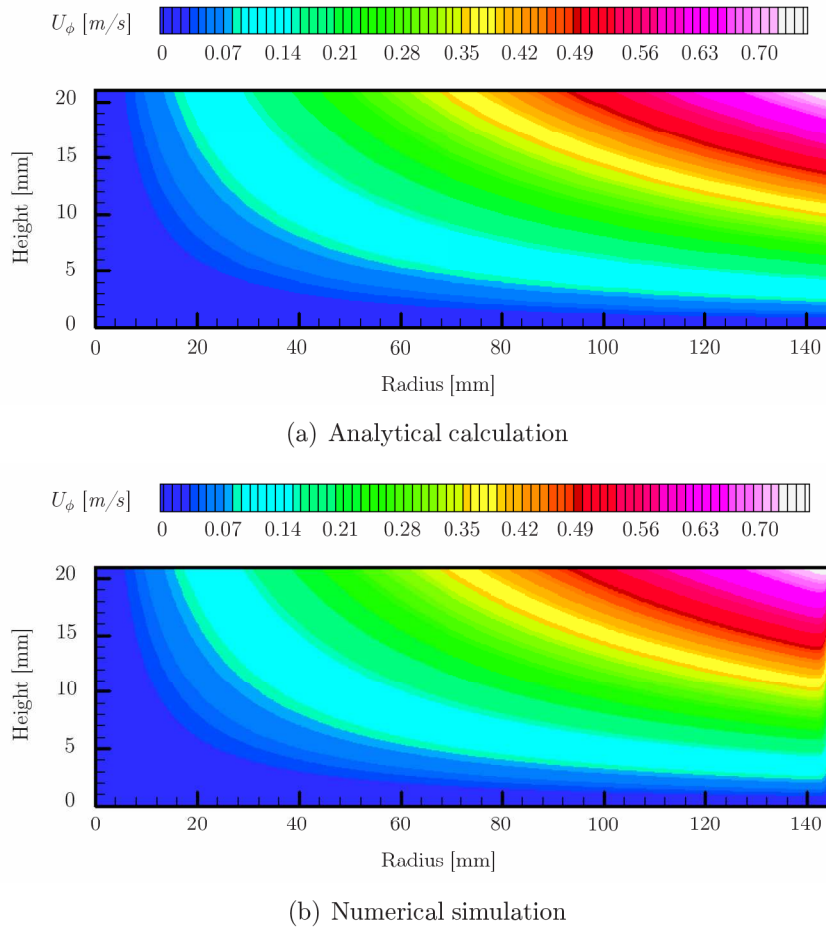

(b) Numerical simulation

Figure 8.21: Swirl velocity distribution of the laminar flow in a vertical plane

In Figure 8.21(a) the solution of this equation is given for a vertical plane at an arbitrary azimuthal angle ϕ. In this figure $r = 0$ mm equals the rotating axis of the disk and $r = 145$ mm the vertical inner wall. The measurement volume is positioned around $r = 99$ mm. As the analytical solution is based on an infinitely large radius, it does not take into account the side wall present in this measurement arrangement. To verify whether this side wall has any effect on the velocity distribution inside the measurement volume, a numerical simulation was conducted using a two-dimensional structured grid in *Fluent*. The resulting velocity field is shown in Figure 8.21(b), where it can be seen that only close to the inner side of the vertical wall, the velocity distribution deviates from the analytical solution, since here the no-slip condition is present. At the positions where the measurement volume is placed, i.e. around $r = 99$ mm, no influence of the side walls is seen, meaning that the analytical solution can be used as a comparison for the experimentally measured velocity distributions.

To get reliable mean velocity fields and standard deviations 3000 image pairs of the particles inside the measurement volume are recorded at a frequency of 3 Hz with a time delay between the laser pulses of each pulse pair of 600 μs. After selecting different layers, the particle images are defined to a certain layer inside the volume. To assure enough particle images for the recordings of each layer, instantaneous averaged recordings are produced by adding twenty pairs of

particle images together for every layer, resulting in 150 instantaneous averaged recordings per investigated layer inside the measurement volume. These averaged recordings are subsequently processed by the data processing software described in section 8.3, resulting in velocity fields at different depths inside the measurement volume. The images are analysed with a window size of 64×64 pixels and an overlap factor of 50%, resulting in an in-plane spatial resolution of 141 μm. The different layers are chosen in such a way that each layer covers a range in central moments ratio of 0.5 inside the total central moments ratio range going from 0.1 to 3.6. This leads to eight slices over the total depth of the investigated film. By using the equations given in Table 8.1 and Table 8.2 for each investigated depth range, the coinciding physical depths in the measurement volume and the theoretical mean velocities (eq. (8.20)) can be obtained. These values are shown in Table 8.3.

Table 8.3: Velocity distribution for the different investigated depth ranges inside the measurement volume (calculated with the equations for μ_{2x}, μ_{2y} and μ of Table 8.2 and 8.1)

Log(μ) [-]	μ_{2x} [-]	μ_{2y} [-]	Physical depth in the measurement volume [mm]	Theoretical mean velocity [mm/s]
-0.72 *to* -0.15	66 *to* 149	215 *to* 447	1.47 *to* 2.10	361 *to* 516
-0.15 *to* 0.08	149 *to* 192	158 *to* 215	1.24 *to* 1.47	305 *to* 361
0.08 *to* 0.23	192 *to* 216	111 *to* 158	1.15 *to* 1.24	283 *to* 305
0.23 *to* 0.34	216 *to* 225	102 *to* 111	1.05 *to* 1.15	258 *to* 283
0.34 *to* 0.43	225 *to* 258	87 *to* 102	0.94 *to* 1.05	231 *to* 258
0.43 *to* 0.51	258 *to* 347	87 *to* 112	0.67 *to* 0.94	165 *to* 231
0.43 *to* 0.51	347 *to* 550	112 *to* 204	0.35 *to* 0.67	86 *to* 165
0.34 *to* 0.43	550 *to* 2300	204 *to* 1500	0 *to* 0.35	0 *to* 86

The obtained in-plane mean velocity fields at the eight slices of the investigated film are shown in Figures 8.22 and 8.23 for, respectively, depths between $z = 0$ mm and 1.05 mm and between $z = 1.05$ mm and 2.10 mm. Here, $z = 0$ mm corresponds to the bottom of the container, hence the vertical position of the non-moving plate. In these images, the colors define the absolute mean velocity values integrated over the depth of each slice, whereas the vectors present the direction of the flow. Despite the low particle density for each layer inside the flow, very clear uniform velocity fields are obtained, as a result of the average correlation method. With the exception of Figures 8.23(c) and 8.23(d), all images show a flow from the top to the bottom, which is consistent with the rotational direction of the plate covering the liquid film. The reason that the mean flow fields at the two most upper layers, i.e. the layers in between $z = 1.24$ mm and 1.47 mm and in between $z = 1.47$ mm and 2.10 mm, are in counter-rotating direction with the rotating plate is unknown. At these heights, by inspection of the recorded images, it is seen that the tracer particles are being imaged correctly and as bright as the images close to the bottom of the film, leading to a clear distinction between the particles at different depths. Furthermore, the density of the RhodamineB PMMA particles is the same as that of the glycerine/water mixture, therefore there exists an equilibrium between the upward buoyancy forces and the gravity forces. In this way, no movement of the particles in vertical direction is to be expected. Since the particles are equally distributed over the depth of the flow, it is not to be expected that the particle number is lower at these heights, what could have led to wrong calculations of the inverse Fourier transformation and incorrect velocity fields.
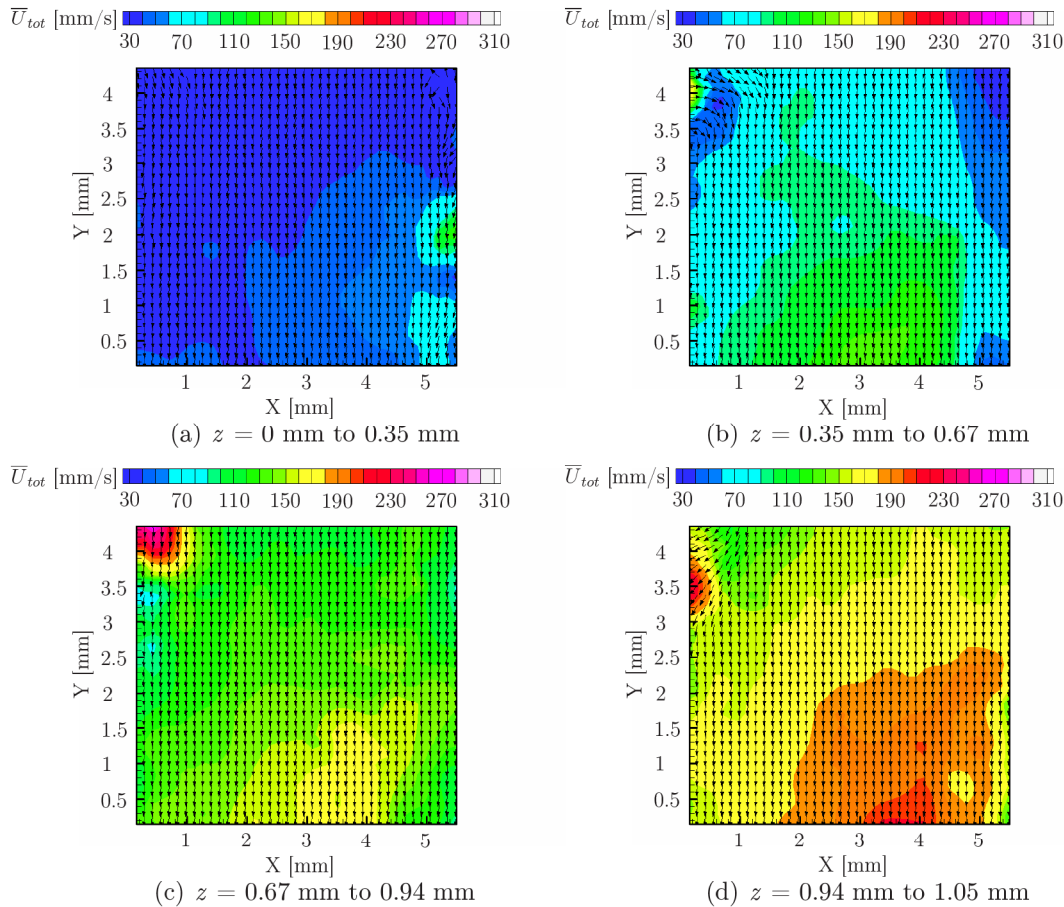
Figure 8.22: In-plane mean velocity distributions at different heights between $z = 0$ mm and 1.05 mm inside the laminar flow

When looking at the in-plane distribution of the mean average velocities for each slice of the flow it is observed that, with the exception of Figures 8.23(c) and 8.23(d), the mean velocities are increasing uniformly when approaching the rotating plate.

These experimentally obtained mean in-plane velocity values are compared with the theoretical velocity values, given by eq. (8.20), and the velocity values obtained with the numerical simulation and the results are shown in Table 8.4 and plotted in Figure 8.24. For most of the layers the measured mean velocities deviate up to 30% from the theoretical and numerically simulated results. This large difference can be explained by the choice of the central moments ratio of the intensity for each particle. For the analysis of the data a background intensity threshold for the data processing algorithm is chosen, which is constant over the whole image. Due to the uneven distribution of the background noise over the recorded particle images, certain particles will be given a higher central moments ratio, resulting in a lower depth determination of these particles; hence, a lower local particle displacement and flow velocity than the theoretical values. This can be overcome by giving each tracer particle in the recordings its own local threshold by optimizing its background intensity level, which has not been applied yet to these tracer particle recordings. Although the background noise plays an important role in the image analysis and causes a large difference between the experimentally obtained mean velocity values and the theory, the experiments capture well the mean velocity fields and values

248